


High-Rate and High-Fidelity Modular Interconnects between Neutral Atom Quantum Processors

Yiyi Li¹ and Jeff D. Thompson^{1*}

Department of Electrical and Computer Engineering, Princeton University, Princeton, New Jersey 08544, USA

 (Received 17 January 2024; accepted 15 May 2024; published 20 June 2024)

Quantum links between physically separated modules are important for scaling many quantum computing technologies. The key metrics are the generation rate and fidelity of remote Bell pairs. In this work, we propose an experimental protocol for generating remote entanglement between neutral ytterbium atom qubits using an optical cavity. By loading a large number of atoms into a single cavity, and controlling their coupling using only local light shifts, we amortize the cost of transporting and initializing atoms over many entanglement attempts, maximizing the entanglement generation rate. A twisted ring cavity geometry suppresses many sources of error, allowing high-fidelity entanglement generation. We estimate a spin-photon entanglement rate of $5 \times 10^5 \text{ s}^{-1}$, and a Bell pair rate approaching 10^5 s^{-1} , with an average fidelity near 0.999. Furthermore, we show that the photon detection times provide a significant amount of soft information about the location of errors, which may be used to improve the logical qubit performance. This approach provides a practical path to scalable modular quantum computing using neutral ytterbium atoms.

DOI: [10.1103/PRXQuantum.5.020363](https://doi.org/10.1103/PRXQuantum.5.020363)

I. INTRODUCTION

The development of a large-scale, fault-tolerant quantum computer capable of solving classically intractable problems is expected to require millions of qubits [1,2]. In many physical computing architectures, it is challenging to imagine scaling a single device to this number of qubits, because of varied constraints including cryogenic cooling power, wiring density, or laser power. These challenges can be circumvented with a modular approach, using remote connections to link together a number of small units into a single quantum processor [3–6]. Modularity may also simplify the construction, maintenance, and calibration of large-scale systems.

The basic building block of a modular computer is a Bell pair between physical qubits in two modules, which can be used as a resource to teleport quantum states or gates between the modules [7–10]. However, it is an outstanding challenge to develop an interface between modules with sufficient bandwidth and fidelity to enable scalable, fault-tolerant computation. In superconducting qubits, proof-of-concept demonstrations have

shown cryogenic microwave links between remote qubits [11], and entanglement between microwave and optical photons [12,13]. Remote entanglement of atomic qubits such as neutral atoms, trapped ions, and solid-state defects using photons has been implemented with several approaches, using free-space and cavity-enhanced light-matter interfaces [8,14–23]. However, the highest reported remote entanglement rate between neutral atom or trapped ion qubits is only 182 s^{-1} , with a fidelity of 0.94 [20].

Quantum processors based on neutral atom arrays have developed rapidly in recent years, scaling to hundreds of qubits [24,25], entanglement fidelities over 0.99 [26,27], and programmable processors [28,29] including logical qubits [30]. Several previous works have considered modular interfaces for neutral atom arrays using optical cavities [31–33], which can be conveniently integrated with the rest of the processor by transporting atoms in moving optical tweezers [28,31,32,34,35].

In this work, we propose an approach to realize fast, high-fidelity remote qubit entanglement between neutral atom quantum processors. We consider ^{171}Yb atoms as qubits, which have been used to demonstrate high-fidelity entangling gates [36], nondestructive [37] and midcircuit [38,39] readout, and have a pathway to hardware-efficient fault-tolerant error correction [40,41]. By using an optical tweezer array to place $N > 100$ atoms inside a single optical cavity (a twisted ring resonator), and controlling their interaction with the cavity using only local light shifts, we predict a remote Bell pair generation rate of

*Corresponding author: jthompson@princeton.edu

Published by the American Physical Society under the terms of the [Creative Commons Attribution 4.0 International](https://creativecommons.org/licenses/by/4.0/) license. Further distribution of this work must maintain attribution to the author(s) and the published article's title, journal citation, and DOI.

$1.0 \times 10^5 \text{ s}^{-1}$ with a fidelity of approximately 0.999 for physically reasonable parameters. The entanglement is distributed between modules using 1389-nm photons in a single-mode optical fiber, allowing links over several kilometers without degradation. We conclude with a brief discussion of how the remote Bell pairs can be used to implement fault-tolerant operations between modules.

This rate is orders of magnitude higher than previously demonstrated [16,18,20,22] or proposed [32,33] remote entanglement approaches for atomic qubits. This approach will enable the development of large-scale quantum processors using neutral atom arrays.

II. OVERVIEW

An overview of the proposed approach is shown in Fig. 1. We envision an array of computation modules each housed in a separate vacuum system containing an optical cavity used to generate spin-photon entanglement. Photons are emitted on the 1389-nm transition from 3D_1 to 3P_0 ($\Gamma = 2\pi \times 418 \text{ kHz}$) [43], with a polarization entangled with the qubit states in 3P_0 . After the photons leave the optical cavity, they are coupled into optical fibers, and sent to a central router and detector array [4]. The router interferes photons coming from selected pairs of modules on an array of beam splitters. The coincident detection of two photons on the same beam splitter heralds the generation of a Bell state, with a success probability of 50%.

The optical cavity within each module is a nonplanar (twisted) ring cavity [Fig. 1(b)] [44], which allows small beam waists with robust alignment [45–47], spatially uniform atom-cavity coupling (i.e., without a standing wave), and nondegenerate modes of opposite circular polarization [48] that are used to couple to two Zeeman-split transitions simultaneously to generate spin-polarization entanglement. This doubles the entanglement generation rate compared to time-bin entanglement when coupling to a single transition.

The operation of the modular interface with a tweezer array is shown in Figs. 1(c)–1(e). An array of N atoms is initialized in a loading zone, then transported into the cavity. Once inside, the entire array is initialized in a superposition state within the 1S_0 ground state $|\psi_0\rangle^{\otimes N} = [(|0_g\rangle + |1_g\rangle)/\sqrt{2}]^{\otimes N}$. The first atom in the array is excited to a superposition state in the $6s5d^3D_1$ manifold, $|\psi_e\rangle = (|0_e\rangle + |1_e\rangle)/\sqrt{2}$, which decays to the qubit state in the 3P_0 manifold, by emitting a 1389-nm photon into the cavity with σ^- or σ^+ polarization. This results in the spin-photon entangled state $|\psi_{sp}\rangle = (|0, \sigma^- \rangle + |1, \sigma^+ \rangle)/\sqrt{2}$. By performing the excitation synchronously in two modules, the emitted photons will arrive simultaneously at the detectors, and an entangled state of two qubits $|\psi^\pm\rangle = (|01\rangle \pm |10\rangle)/\sqrt{2}$ is heralded when two photons of opposite polarization are detected [49].

The process is repeated sequentially for each atom in the array, with a delay of $t_{\text{ent}} \approx 1 \text{ }\mu\text{s}$ to ensure that the photon wavepackets do not overlap. After exciting all of the atoms once, the procedure can be repeated $m \approx 5\text{--}10$ times to boost the entanglement fraction, by reinitializing the atoms that were not successfully entangled in previous rounds [Fig. 1(e)]. After a sufficient number of Bell pairs are generated, the array is moved out of the cavity and replaced by a fresh array to continue generating more Bell pairs. By amortizing the relatively high temporal cost of moving ($t_{\text{move}} \approx 100 \text{ }\mu\text{s}$ [28]) and initialization ($t_{\text{init}} \approx 6\text{--}8 \text{ }\mu\text{s}$) over many repetitions of the entanglement sequence, the average spin-photon entanglement attempt rate approaches the maximum allowed by the cavity, $1/t_{\text{ent}}$. Saturating this rate requires $N \gtrsim (t_{\text{move}} + t_{\text{init}})/t_{\text{ent}} \approx 100$. Locally addressed light shifts of the 3D_1 state prevent reabsorption of photons by atoms already in 3P_0 .

The subset of qubits that were successfully entangled can be used to perform remote operations between logical qubits $|\psi_L\rangle$ in two modules, for example by using teleported gates to implement lattice surgery or transversal entangling gates [50].

III. ENTANGLEMENT RATE

An example cavity design is shown in Fig. 1(b), consisting of four mirrors in a twisted ring. The large spacing between the mirrors and the atoms eliminates unwanted atom-surface interactions and provides ample optical access for optical tweezers, imaging, and gate beams. The twisted geometry breaks the degeneracy of modes with opposite helicity [48], resulting in a controllable splitting between copropagating modes with σ^+ and σ^- polarization. The twist angle of approximately 11° is chosen to tune the forward-propagating modes into resonance with the transitions from $|0\rangle$ and $|1\rangle$ to 3D_1 simultaneously, in a bias field of 100 G ($\omega_+ - \omega_- = 140 \text{ MHz}$). The mirror radius of curvature and arm lengths are chosen to provide a circular mode with a $1/e^2$ waist $w_0 = 10 \text{ }\mu\text{m}$ at the position of the atoms. This results in a peak atom-cavity coupling strength of $g_{\text{max}} = 2\pi \times 520 \text{ kHz}$ for both transitions, and provides space for an array of $N = 204$ atoms with $g > 0.9g_{\text{max}}$ [Fig. 2(a)]. The round-trip length is $L = 6.96 \text{ cm}$, corresponding to a free spectral range of 4.3 GHz, and the cavity decay rate κ is chosen by selecting the reflectivity of the outcoupler mirror (the other mirrors have $R = 1$). Additional details about the cavity design can be found in Appendix B.

The procedure for generating the spin-photon entangled state $|\psi_{sp}\rangle$ is as follows. After preparing the array in $|\psi_0\rangle^{\otimes N}$, we use a two-photon excitation pulse with Rabi frequency $\tilde{\Omega} = \Omega_{1\pm}\Omega_{2\pm}/2\Delta_{\pm}$ to excite a single atom to $|\psi_e\rangle$. The atom decays by emission into the cavity and free-space modes, and the cavity output is shown in Fig. 2(b). To avoid residual population in the cavity causing an error

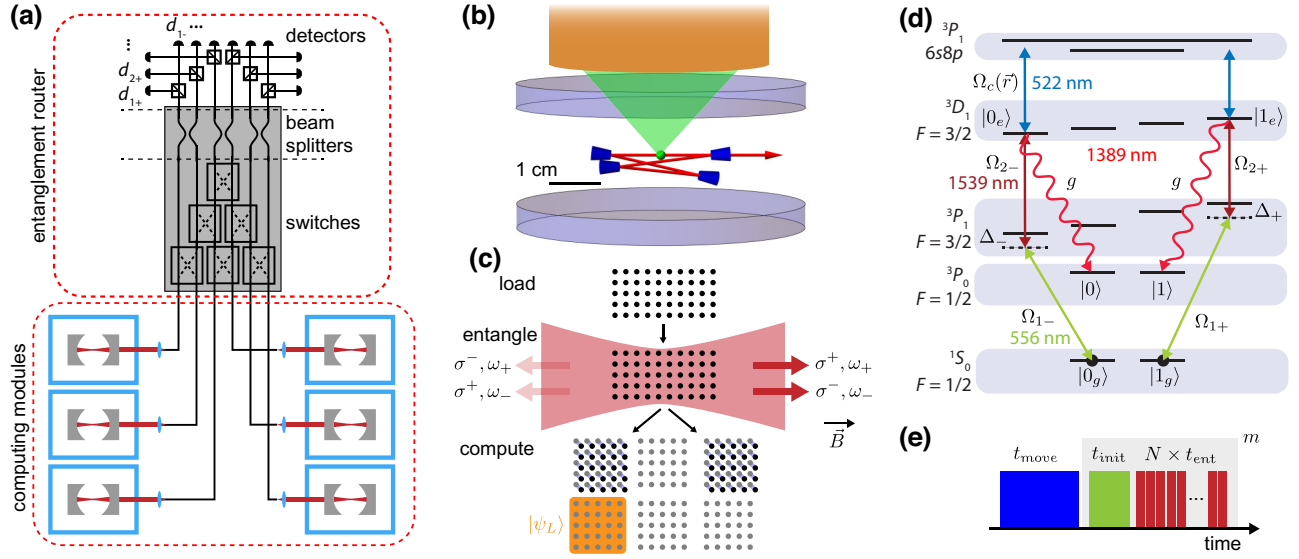


FIG. 1. (a) Schematic of a modular neutral atom quantum computer with multiple computation modules and a central entanglement router. (b) Each module houses a centimeter-scale twisted ring cavity, shown here with vacuum windows and a high-NA microscope objective with standard dimensions for scale [42]. (c) The entanglement process consists of loading and transporting arrays of atoms into the cavity, entangling them sequentially with a remote module, and moving them into a computation zone. There, they can be used to connect remote logical qubits $|\psi_L\rangle$ using teleported gate operations. (d) Energy diagram of relevant atomic levels in ^{171}Yb . The qubit state used for computation is in the 3P_0 manifold. The atoms are excited from the 1S_0 ground states to the 3D_1 states with a two-photon excitation using 3P_1 as an intermediate state. The Rabi frequencies of the excitation lasers are $\Omega_{1\pm}$ and $\Omega_{2\pm}$, with detuning to the intermediate state of Δ_{\pm} . The 3D_1 to 3P_0 transitions are coupled to the cavity with an atom-cavity coupling strength of g . Local light shifts are applied to selected atoms, using $\Omega_c(\vec{r})$ coupling 3D_1 to a higher excited state. (e) Temporal sequence of remote entanglement generation: by amortizing the cost of moving and initializing atoms over many entanglement attempts, the overall attempt rate is very close to $1/t_{\text{ent}}$.

on the next entanglement attempt, one would have to wait for a time $t > 5/\Gamma$. However, the exponential tail can be suppressed by tuning the atom out of resonance with the cavity suddenly at $t = \pi/g$, when the cavity population vanishes, using a strong light shift Δ on the 3D_1 state with $\Delta/g > 100$. This traps the residual excitation in the atom, where it decays into free-space modes, and allows the next atom to be excited to 3D_1 immediately, doubling the emission rate to $t_{\text{ent}} = 2.65/\Gamma$, while decreasing the emission probability per attempt by only 1%. The light shift is kept on for the remainder of the sequence, to prevent atoms in 3P_0 from absorbing cavity photons from subsequent entanglement attempts. After attempting to entangle all N atoms, the atoms that were not entangled can be repumped back to $|0_g\rangle$, and the entire procedure repeated for another round.

Figure 2(c) shows the probability of emission into the cavity as a function of κ , reaching a maximum of $\eta = 0.50$ when $\kappa/2\pi = 1.04$ MHz (corresponding to a cavity finesse of $\mathcal{F} = 2070$). This does not achieve the maximum possible efficiency $\eta_0 = C/(1+C)$, where $C = 4g^2/(\kappa\Gamma) \approx 2.5$ is the cooperativity, because the cavity becomes spectrally narrower than the emitted photon when κ is small [33]. Adiabatic preparation of a shaped photon pulse can saturate η_0 [51] by increasing t_{ent} , but we have found that

this does not increase the remote entanglement rate and adds significant additional experimental complexity.

Each entanglement attempt heralds a successful Bell pair with probability $P_{\text{suc}} = (1/2)\eta^2 = 0.125$. Using the sequence in Fig. 1(e), the average Bell pair rate when using m rounds is

$$R_{\text{bp}} = \frac{\sum_{i=1}^m N_i P_{\text{suc}}}{t_{\text{move}} + m t_{\text{init}} + \sum_{i=1}^m N_i \bar{t}_{\text{ent}}}, \quad (1)$$

where $N_i = N_{i-1}(1 - P_{\text{suc}})$ is the number of entanglement attempts in round i ($N_1 = N$), and $\bar{t}_{\text{ent}} = 1.09 \mu\text{s}$ is the average time per entanglement attempt across the $N = 204$ site array. After one round ($m = 1$) the rate is $7.8 \times 10^4 \text{ s}^{-1}$, increasing to $1.0 \times 10^5 \text{ s}^{-1}$ for $m = 5$ – 20 rounds. This is 82% of the maximum rate allowed by the cavity, $P_{\text{suc}}/t_{\text{ent}} = 1.25 \times 10^5 \text{ s}^{-1}$, indicating the effectiveness multiplexing the cavity across N atoms. Photon loss in the propagation and detection path will reduce the entanglement generation rate. With state-of-the-art mode matching [52] and photon detection efficiency [53], we project a realistic Bell pair generation rate of $8.8 \times 10^4 \text{ s}^{-1}$ between two modules. We also note that large switch networks have been demonstrated with average loss of

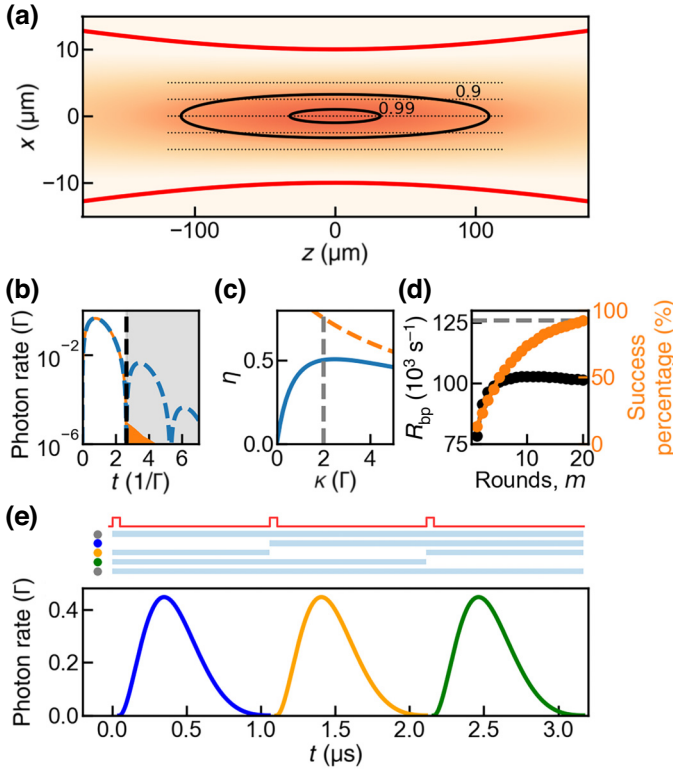


FIG. 2. Entanglement rate. (a) Schematic of an atom array inside the cavity. The red contour indicates the $1/e^2$ intensity of the cavity field, while the black lines show $g = 0.99g_{\max}$ and $g = 0.9g_{\max}$. The dots depict an atom array with a spacing of $2.5 \mu\text{m}$, which allows $N = 204$ sites to fit inside the $0.9g_{\max}$ contour. (b) Output intensity from the cavity after exciting an atom to 3D_1 (blue dashed line). A light shift Δ applied at $t \approx \pi/g = 2.65/\Gamma$ suppresses the late time decay (orange line, $\Delta/g = 100$), allowing the next atom to be excited immediately. (c) Probability of emission into the cavity, η , as a function of the cavity decay rate, κ (blue). The orange curve shows the maximum possible value, $\eta_0 = C/(C+1)$. The optimum κ is indicated by the vertical line, where $\eta = 0.50$. (d) Bell pair generation rate R_{bp} and the percentage of atoms entangled, as a function of the number of rounds, m . (e) Timing diagram for the entanglement sequence in a small array, showing the local light shifts (blue bars), global excitation pulses (red), and cavity output field. Note that at each point in time, a light shift is applied to all atoms *except* for the one being entangled.

1.33 dB [54], which further reduces the Bell pair generation rate to $4.9 \times 10^4 \text{ s}^{-1}$ between any two modules in the network.

The same light shift control can also be used to address the excitation and repumping operations, as described in Appendix A. A timing diagram of part of one round is shown in Fig. 2(e).

IV. ENTANGLEMENT FIDELITY

Next, we consider errors affecting the fidelity of the remote Bell pairs. Previous experimental studies of heralded entanglement based on coincidence detection have

identified errors arising from qubit decoherence, the fidelity of single-qubit rotations, polarization mixing, and imperfect mode overlap at the detectors [18,20].

The latter effects are strongly suppressed by the cavity. The mode structure of the cavity ensures that the photons are emitted into a single, well-defined mode with orthogonal polarizations, which can be preserved through the entanglement router by using fiber optic or integrated photonic beam splitters with extremely low loss at this wavelength [55].

Furthermore, the excellent coherence and high-fidelity single-qubit operations on the nuclear spin qubit in ^{171}Yb largely mitigates the first two effects. Coherence times without dynamical decoupling (i.e., T_2^*) of several seconds have been demonstrated for the pure nuclear spin qubit in 1S_0 and 3P_0 , because of the low sensitivity to magnetic field noise and the absence of differential light shifts [36,38,56,57]. The 3P_0 state lifetime is 3 s in typical optical tweezers [36], resulting in a decay probability to 1S_0 of 7×10^{-7} per t_{ent} or 2×10^{-4} over $m = 5$ sequence repetitions with $N = 204$ atoms. We also note that 3P_0 decays can be converted into erasure errors, which can be efficiently corrected [36,40]. Unlike 3P_0 and 3S_0 , the 3D_1 state is sensitive to magnetic fields. However, it is only populated for approximately $1 \mu\text{s}$ during the entanglement generation, compatible with phase accumulation errors less than 10^{-6} using conventional field stabilization at the part-per-million level [58]. Single-qubit gates for both 1S_0 and 3P_0 qubits have been demonstrated with fidelities beyond 0.999 [36,38,56,57].

Now, we turn to some sources of error that are intrinsic to our implementation. The magnitude of these error sources is estimated from numerical simulations (Appendix C) unless otherwise stated. The first is a slight distinguishability of the photons from two atoms resulting from variations in the atom-cavity coupling strength. Given two atoms in two cavities with a fractional difference in coupling strength δ_g/g , the resulting distinguishability causes an error $\epsilon_g = 0.394 \times (\delta_g/g)^2$, such that $\delta_g/g < 0.05$ is required to reach $\epsilon_g < 10^{-3}$ [Fig. 3(a)]. Maintaining an rms variation in g below this level for all possible qubit pairs requires matching the cavity waists within 5%, and placing the atoms within $0.4w_0 \approx 4 \mu\text{m}$ of the cavity axis [compatible with the layout in Fig. 2(a)]. Static inhomogeneity in g can also be mitigated by misaligning the atoms in one cavity, or choosing matched pairs of atoms to entangle. However, unknown variation in g can arise from thermal motion of the atoms or alignment drifts between the tweezer array and the cavity. Thermal motion at $10 \mu\text{K}$ corresponds to $\delta_g/g \approx 3 \times 10^{-3}$, while maintaining $\delta_g/g < 0.05$ requires alignment stability to within $(\Delta x, \Delta y, \Delta z) < (0.87, 2.2, 3.8) \mu\text{m}$, compatible with demonstrated tweezer alignment stability to nanophotonic structures [35] and standing-wave lattices [59]. Variation in κ has a similar effect as variation in g : a

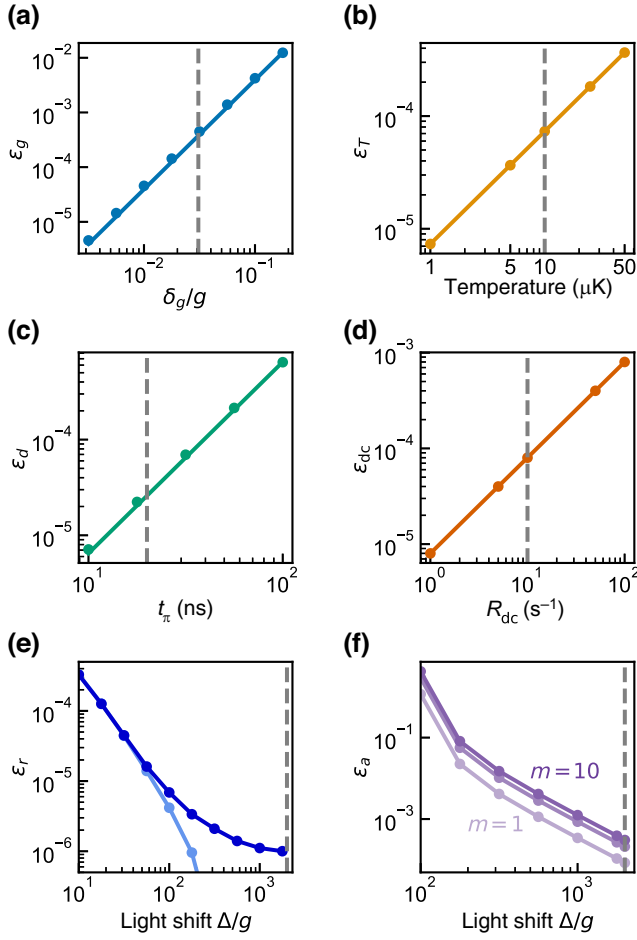


FIG. 3. (a) Error resulting from an unequal atom cavity coupling strength, ϵ_g . The dashed line shows a representative value, $\delta_g/g = 0.031$, derived from the rms variation across the array shown in Fig. 2(a). (b) Doppler shift error, ϵ_T , from finite atomic temperature. The dashed line shows a typical temperature for Yb atoms after Doppler cooling. (c) Error from re-excitation of the atom following a decay during the excitation pulse, ϵ_d . (d) Error from detector dark counts, ϵ_{dc} . (e) Error probability from the residual cavity photon population after each entanglement attempt, ϵ_r , as a function of the light shift detuning Δ/g . The light line shows the case that g is known exactly, while the dark line includes an uncertainty in g of $\delta_g/g = 3 \times 10^{-3}$, corresponding to thermal atomic motion at $T = 10 \mu\text{K}$. (f) The error probability ϵ_s from scattering or Stark shifts from cavity photons in subsequent rounds, as a function of the light shift detuning Δ/g . Purple lines show the error after $m = 1, 5, 10$ rounds (from light to dark).

10% mismatch in κ between two cavities results in an error of 1.6×10^{-4} .

Distinguishability errors can also arise from Doppler shifts, given the running-wave mode in the cavity. The error probability ϵ_T is proportional to $(k_c v_{\text{rms}}/g)^2$, where $k_c = 2\pi/\lambda$ is the cavity wave vector, and $v_{\text{rms}} = \sqrt{k_B T/m}$ is the mean atomic velocity along the cavity axis (with k_B , T , and m denoting Boltzmann's constant, the atomic

temperature, and the mass of the atom, respectively). From numerical simulations, we find that $\epsilon_T = 7.3 \times 10^{-6} \mu\text{K}^{-1} \times T$ [Fig. 3(b)]. A typical temperature for Yb atoms after Doppler cooling is 5–10 μK [36,42,57], corresponding to $k_c v_{\text{rms}} = 2\pi \times 16 \text{ kHz}$, yielding $\epsilon_T < 10^{-4}$. We note that this error could be further suppressed using ground-state cooling, which is readily achievable in Yb [57,60].

Next, we consider decay back to 1S_0 during the excitation pulse, which collapses the initial spin superposition, but can still result in photon emission into the cavity if the atom is re-excited. The 3D_1 state decays to 3P_1 with a branching ratio of 0.34, and 3P_1 decays to 1S_0 at a rate $\Gamma_3 = 2\pi \times 182 \text{ kHz}$. Therefore, the probability to decay to 1S_0 during an excitation pulse of duration $t_\pi \ll \Gamma, \Gamma_3$ is $p_3 \approx 0.34 t_\pi^2 \Gamma_3 \Gamma$. The probability of the atom being re-excited and causing an error is $\epsilon_d \approx p_3/8$. From numerical simulations, we find that $\epsilon_d = 6.8 \times 10^{-8} \text{ ns}^{-2} \times t_\pi^2$, which yields $\epsilon_d = 2.8 \times 10^{-5}$ for $t_\pi = 20 \text{ ns}$. In Appendix A, we discuss errors from unwanted excitation to $^3D_1, m_F = \pm 1/2$ levels and off-resonant scattering from 3P_1 , which can both be suppressed below this level.

Then, we consider decay false heralding events from detector dark counts [Fig. 3(d)]. The probability of a false coincidence from detecting a signal and background photon simultaneously is $p_f = 2\eta R_{dc} t_{\text{ent}}$, where R_{dc} is the dark count rate on a single detector. Therefore, the probability of an error caused by the dark count is $\epsilon_d = p_f/P_{\text{suc}} = 4t_{\text{ent}}R_{dc}/\eta \approx 8 \times 10^{-6} \text{ s} \times R_{dc}$. Commercially available superconducting nanowire single-photon detectors have a dark count rate $R_{dc} = 10 \text{ s}^{-1}$, corresponding to an error probability of $\epsilon_{dc} = 8 \times 10^{-5}$. Suppression to millihertz rates has been demonstrated using cold filtering [61] or integrating the detector to a single-mode waveguide [62].

Finally, we consider errors from the presence of multiple atoms inside the cavity. These errors take two forms: residual photons in the cavity at the end of one entanglement attempt leaking into the next window, and atoms already in 3P_0 absorbing a photon if they are not sufficiently light shifted away from the cavity resonance [Fig. 3(f)]. If the atom-cavity coupling is known exactly, the residual photon errors are suppressed by the light shift as $\epsilon_r \propto (\Delta/g)^{-2}$, provided that the light shift is turned on instantaneously at the time when the cavity population is zero [Fig. 3(e)]. However, unknown variation in g and the finite rise time of the modulator used to generate the light shift makes this precise timing impossible. Using the uncertainty $\delta_g/g = 3 \times 10^{-3}$ from thermal atomic motion at 10 μK , and assuming a 10-ns rise time for the light shift pulse, we find a floor of $\epsilon_r < 10^{-5}$ with a light shift of $\Delta/g > 100$.

Atoms already in 3P_0 after a successful entanglement attempt can experience scattering or Stark shifts from photons in the cavity during subsequent entanglement

attempts. Both errors are suppressed with the light shift as $(\Delta/g)^{-2}$, and we find from numerical simulations that the error probability after one additional entanglement attempt is $\epsilon_a^{(1)} = 3.5 \times (\Delta/g)^{-2}$. However, because the error is incurred on the atom that was already entangled, the average generated Bell pair will experience $\bar{N}_r = \mathcal{O}(mN)$ subsequent entanglement attempts before being transported out of the cavity, amplifying its effect. For $N = 204$ and $m = 5$, we numerically find that $\bar{N}_r \approx 250$. Achieving an average error $\epsilon_a = \bar{N}_r \epsilon_a^{(1)} < 10^{-3}$ requires $\Delta/g > 2 \times 10^3$. We note that ϵ_a grows sublinearly with m , and is therefore not very sensitive to the number of rounds, similar to R_{bp} in Eq. (1).

Adding the above sources of error, we arrive at an average Bell pair fidelity of approximately 0.999, dominated by ϵ_a and ϵ_g .

We note that only a modest amount of laser power is required for the light-shifting beam when operating close to resonance on the 3D_1 to $6s8p\ ^3P_1$ transition. As demonstrated in Ref. [63], working close to resonance is possible because the 3D_1 state is not populated on the shifted sites, and therefore insensitive to scattering errors. With a target error of ϵ , the optimal detuning of the light-shifting beam is suggested to be $\Gamma/\sqrt{\epsilon}$, where Γ is the linewidth of the transition used for applying a light shift. Aiming for an error of $\epsilon \approx 10^{-4}$, the optimal detuning is around 1 GHz for the light-shifting beam. Using a 1-GHz detuning, a laser power of approximately 20 μW per atom is sufficient to generate a light shift on the 3D_1 state of $\Delta/g > 2 \times 10^3$, with negligible mechanical forces on the atoms as the wavelength is far from resonance with any transitions from 1S_0 or 3P_0 . Unwanted light shifts on the atom being entangled can arise from crosstalk of the local addressing beam, and lead to distinguishability errors similar to Doppler shifts. A recently demonstrated large-scale modulator achieves -44-dB nearest-neighbor crosstalk [64], which would give a detuning error 2.6 times the rms Doppler shift, or an entanglement error of 5×10^{-4} .

A. Information about errors from photon timing

In the context of quantum error correction, the details of the error model can significantly affect the overhead required to reach a given logical error rate. For example, a bias towards a single type of Pauli error [65,66] or information about the location of errors in the form of erasures [40,41,67,68] or soft information [69] have been shown to reduce logical error rates by several orders of magnitude. While many quantum operations can only be characterized by their average fidelity, here we show that the timing of the photon detection events provides shot-to-shot information about the probability of different error types of each individual Bell pair.

Specifically, we ask the question: given that two photons are detected at times (t_1, t_2) , what is the probability that the

resulting qubit state has a Pauli or leakage error? Since the qubit manifold in ^{171}Yb has only two sublevels, leakage refers to the case that the atom is not in 3P_0 .

First, we consider the errors caused by photon distinguishability from a variation in the atom-cavity coupling strength. This results in unequal wavepacket shapes for the two photons, which encodes which-path information into the detection time difference. These errors are purely Pauli-Z errors, as the correlation between the photon polarization and the qubit state in the computational basis is not affected. In Fig. 4(a), we plot the error probability as a function of the photon detection times, $\epsilon_g(t_1, t_2)$. Using the probability to detect photons at those times, $P(t_1, t_2)$, we can convert $\epsilon_g(t_1, t_2)$ into a probability distribution for the error rate of the generated Bell pairs, $p(\epsilon_g)$, whose cumulative distribution function is shown in Fig. 4(d). The function $p(\epsilon_g)$ gives the probability that a particular Bell pair has a fidelity $1 - \epsilon_g$. While the mean error rate is 4×10^{-4} , over half of the Bell pairs have an error rate less than 6×10^{-5} . This approximates an erasure error and allows for better decoding and improved logical qubit performance.

A similar analysis applies to errors from Doppler shifts. The probability of error as a function of the photon detection times, $\epsilon_T(t_1, t_2)$, is shown in Fig. 4(b). As Doppler shifts also only affect the distinguishability of the photons, this only results in Z errors, and is suppressed when $|\Delta\omega(t_1 - t_2)| \ll 1$, where $\Delta\omega$ is the frequency difference of the two atoms [70]. The cumulative distribution for $p(\epsilon_T)$ is shown in Fig. 4(d).

Errors from decay during the excitation pulse, ϵ_d , can be understood as a Z-basis measurement of the atom prior to the spin-photon entanglement, and are also purely Z errors. However, the photon detection timing does not reveal anything about the probability of this error, so it is the same for all Bell pairs and the cumulative distribution is a step function [Fig. 4(d)].

Dark counts result in false heralding signals that are uncorrelated with the atomic state, and can therefore cause all Pauli errors and leakage. The error probability $\epsilon_{\text{dc}}(t_1, t_2)$ depends on the detection time, and is greatest at the edge of the detection window when the probability of detecting a real photon is low [Fig. 4(c)]. The corresponding cumulative distribution functions for Z, X, and leakage errors is shown in Figs. 4(d)–4(f).

Finally, we consider errors from the absorption of photons by atoms already in Bell pairs, ϵ_a . Because this error happens after the Bell pair is created, it does not depend on the photon detection times. However, Bell pairs created in early rounds have more chances to experience an error than Bell pairs from later rounds. Using the known probability distribution for the number of entanglement attempts N_r that follow a successful Bell pair creation, we can generate the probability distribution $p(\epsilon_a)$ for Z, X, and leakage errors [Figs. 4(d)–(f)]. Because the atom is detuned far

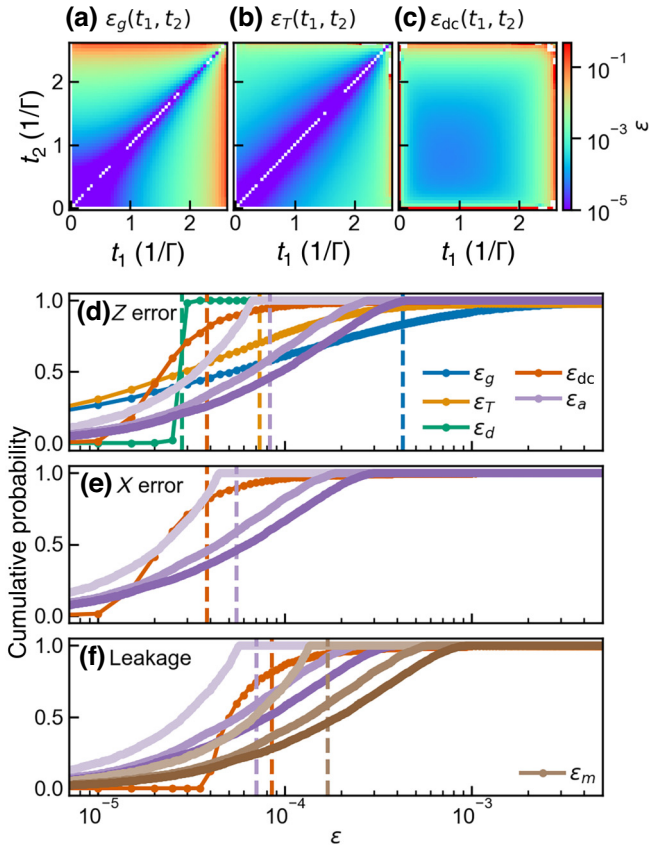


FIG. 4. (a) Probability of an error from unequal g , as a function of the photon detection times (t_1, t_2) . (b) Probability of an error from Doppler shifts as a function of detection times. (c) Probability of a dark count error as a function of photon detection times. (d)–(f) Cumulative probability distribution functions for the Z , X , and leakage error rates for all error sources considered. The dashed lines show the mean probability of each error. For ϵ_a and ϵ_m , the (light, medium, dark) curves show the error probability using $m = (1, 5, 10)$ rounds of entanglement generation, and the dashed line shows the mean error for $m = 5$. For all error types, the strength of the noise corresponds to the dashed vertical lines in Fig. 3, and ϵ_m is computed based on a 3-s lifetime for 3P_0 [36].

from the cavity, the probabilities to excite to all m_F levels of 3D_1 are comparable, and therefore the probabilities of X , Z , and leakage errors are also roughly comparable. Errors from the finite 3P_0 lifetime, ϵ_m , are purely leakage, and follow a similar probability distribution [Fig. 4(f)].

In summary, we have shown that the fidelity of individual Bell pairs is strongly influenced by information that is available to the experimenter: the photon detection times, and the time step in the sequence when the Bell pair was generated. Passing this information to the decoder when performing logical operations may significantly reduce the logical error rate [40,69]. We leave a detailed analysis to future work.

V. DISCUSSION

We conclude by discussing several aspects of these results. First, we note that the proposed approach is fully compatible with existing neutral atom quantum processors. The cavity allows for a large separation between the atoms and the mirror surfaces, comparable to standard glass cell vacuum chambers [42]. It also provides large optical access, compatible with high-numerical-aperture objective lenses for projecting tweezer arrays and local addressing beams, and for fluorescence imaging. Moreover, the steps involved in generating entanglement can proceed in parallel with computations using metastable qubits in a nearby zone, without the need to separately control magnetic fields. The local addressing requirement is minimal, consisting of only one switchable light shift on each site, and is compatible with recently demonstrated scalable modulators [64,71].

Second, we consider how physical Bell pairs can be used to implement fault-tolerant operations between remote logical qubits. Previous studies have considered modular quantum computing in the regime where the modules are small, and a single logical qubit spans multiple modules [4,6,49,72]. While the existence of a high error threshold of over 10% has been demonstrated for the intermodule links [5,6], remote Bell pairs are consumed at a high rate just to sustain the logical information against idle errors.

In the case of neutral atom quantum computing, we envision modules with $\mathcal{O}(10^4)$ qubits per module, based on demonstrated arrays of hundreds of qubits [24,25] and scaling of the underlying optical components beyond 10^4 sites [64]. With foreseeable error rates below 10^{-3} for all physical operations [26,27,36,38], achieving logical error rates of 10^{-12} is possible with an overhead of 10^3 physical qubits per logical qubit using a standard surface code [73]. The overhead may be reduced by at least another order of magnitude using qubits engineered for erasure-biased errors [40,41] or efficient block codes [74]. Therefore, $N_L \gtrsim 100$ logical qubits per module is realistic. In this regime, the remote Bell pairs are not used to correct idle errors and errors from local operations within each module, but only for performing logical operations between modules.

For a distance d surface code, a gate operation between remote logical qubits can be implemented via lattice surgery [50], consuming d^2 physical Bell pairs to teleport controlled-NOT (CNOT) gates along the code boundary [75]. Alternatively, the same number of Bell pairs can be used to implement a logical transversal CNOT across two modules, by teleporting CNOT gates between corresponding physical qubits in the code. The second approach can also be applied to $[[n, k, d]]$ quantum low density parity check codes [76] with a transversal $\text{CNOT}^{\otimes k}$ gate to generate k entangled logical qubits between two modules by consuming n physical Bell pairs, allowing a higher rate

of logical Bell pair generation than the surface code. The implementation of such codes for neutral atom qubits has been discussed in Ref. [74]. As the fidelity of remote physical Bell pairs is similar to those that could be created within a module, intermediate purification steps before using the Bell pairs in logical operations may not be required [6].

Therefore, the physical interface proposed here will enable $\gtrsim 10^3$ remote logical gates per second between each pair of modules. It is an interesting question for future work to consider how to compile high-level algorithms into such a modular computer [1,3,4].

VI. CONCLUSION

We have presented a blueprint for a modular architecture for a neutral atom quantum processor based on Yb atoms. It is capable of generating remote entanglement at a rate of 1.0×10^5 Bell pairs per second, with a fidelity compatible with fault-tolerant computing. The modular interface can be implemented with existing experimental hardware, and operated alongside an atom array performing local computations.

ACKNOWLEDGEMENTS

We gratefully acknowledge Jon Simon for sharing details about computing the normal modes of twisted resonators. We also acknowledge Nathan Schine, Mehmet Uysal, Shruti Puri for helpful discussions, and Adam Kaufman for comments on the manuscript. This work was supported by the Gordon and Betty Moore Foundation (Grant DOI 10.37807/gbmf12253).

APPENDIX A: EXPERIMENTAL SEQUENCE

A detailed description of the experimental sequence is shown in Fig. 5. Here, we discuss each of the steps in additional detail.

After moving atoms into the cavity, the entanglement sequence begins with initializing the array to state $|\psi_0\rangle$. This has two steps: optical pumping to $|0_g\rangle$ on the 1S_0 to 1P_1 transition at 399 nm (requiring less than 100 ns), and a Raman $\pi/2$ rotation (170 ns [57]). We note that these steps do not affect qubits in 3P_0 , so can be used in subsequent rounds without affecting Bell pairs that have already been created.

Then, the atoms are sequentially excited to 3D_1 , using the laser configuration in Fig. 1(d). It consists of three laser beams: a σ_+ -polarized laser driving $|1_g\rangle$ to the $^3P_1, m_F = +3/2$ state with detuning Δ_+ , a σ_- -polarized laser driving $|0_g\rangle$ to the $^3P_1, m_F = -3/2$ state with detuning Δ_- , and a π -polarized laser driving the 3P_1 states to $|0_e\rangle, |1_e\rangle$. Simultaneous two-photon resonance is achieved for both transitions by controlling the frequency of the σ^\pm lasers separately. The two-photon Rabi frequency is given by $\tilde{\Omega}_\pm = \Omega_{1\pm}\Omega_{2\pm}/2\Delta_\pm$. The same laser configuration will

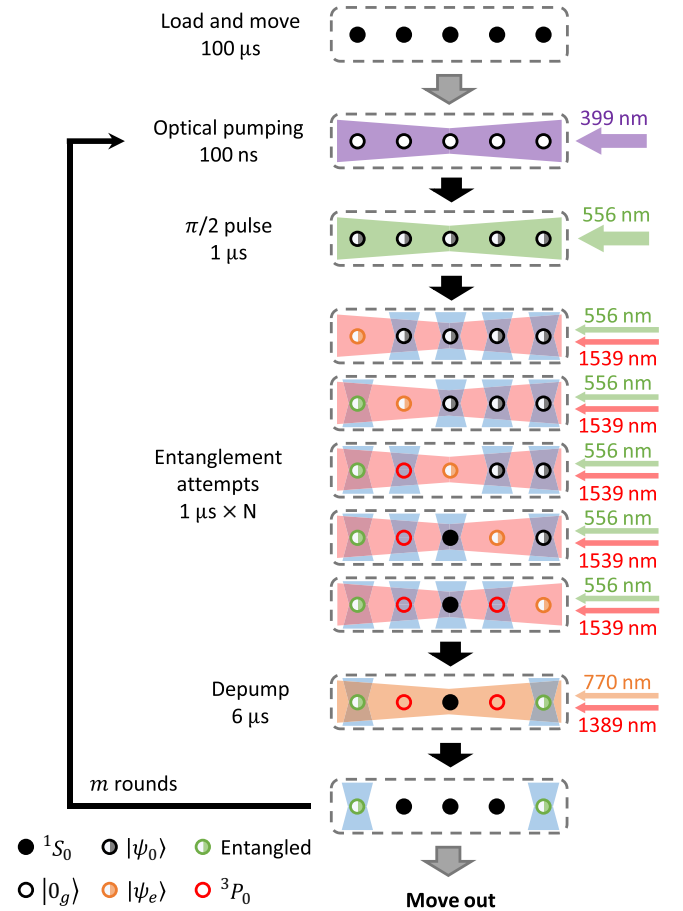


FIG. 5. Schematic diagram of the experimental sequence on a five-atom array.

also drive off-resonant Rabi oscillations to the $^3D_1, m_F = \pm 1/2$ states, with Rabi frequency

$$\tilde{\Omega}'_{\pm} = \sqrt{(g_D \mu_B B)^2 + \left(\frac{1}{3\sqrt{3}} \frac{\Omega_{1\pm} \Omega_{2\pm}}{2(\Delta_{\pm} \pm g_P \mu_B B)} \right)^2}, \quad (\text{A1})$$

where $g_P = 1$ is the $^3P_1, F = 3/2$ state Landé g factor, $g_D = 1/3$ is the $^3D_1, F = 3/2$ state Landé g factor, and μ_B is the Bohr magneton. To minimize off-resonance excitation, the excitation pulse time t_π should be an integer multiple of the off-resonance Rabi cycle, $t_\pi = \pi/\tilde{\Omega}'_{\pm} = l \cdot 2\pi/\tilde{\Omega}'_{\pm}$, where l is an integer. For $\Delta_{\pm} = 2\pi \times 1$ GHz and $B = 100$ G, we numerically found that the minimum pulse time approximately satisfying this condition is $t_\pi \approx 20$ ns. It cannot be exactly satisfied because $\tilde{\Omega}'_{+} \neq \tilde{\Omega}'_{-}$, but the resulting excitation probability to $m_F = \pm 1/2$ is only 3×10^{-6} . This t_π requires $\Omega_{1\pm} = \Omega_{2\pm} \approx 2\pi \times 225$ MHz. The large detuning suppresses scattering from 3P_1 during the pulse to $\Gamma_3/\Delta_{\pm} \approx 10^{-4}$.

Instead of locally addressing the excitation lasers, which atom is excited can be controlled using a local light shift

on 3D_1 during the excitation pulse to shift all but one atom out of resonance. This introduces several new sources of error, which we discuss only briefly because they are not intrinsic (i.e., they can be eliminated by locally addressing at least one of the excitation beams). As discussed in the main text, a value $\Delta/g = 2000$ (corresponding to $\Delta \approx 2\pi \times 1$ GHz) is needed to avoid crosstalk between atoms in the cavity. This is sufficient to suppress unwanted excitation: the probability of a scattering error from 3D_1 during the excitation pulse on a shifted site is approximately $t_\pi \Gamma (\Omega/\Delta)^2 = 3 \times 10^{-5}$. However, both this error and the scattering error from the 3P_1 intermediate state will accumulate, and are enhanced by N for the final atom in each round. This can be suppressed by periodically reinitializing the atoms remaining in 1S_0 in the middle of each round, which adds little temporal overhead, but will eventually heat the atoms from scattering optical pumping photons.

Even on light-shifted sites, the excitation laser can cause vacuum-stimulated Raman transitions resulting in the emission of a photon into the cavity modes. This coherent process occurs at a rate $g\Omega/\Delta \ll \Omega$, resulting in an emission probability of $(g/\Delta)^2 \approx 2 \times 10^{-7}$ per atom during the excitation pulse. This will have the same effect as a dark count or residual photons in the cavity from the previous round. Even when this probability is enhanced by the $N \approx 200$ 1S_0 atoms in the array, it remains well below the other sources of error discussed in the main text.

At the end of the each round, the atoms that are not in Bell pairs need to be depumped from 3P_0 before a new round can start. This can be done conveniently using the 3D_1 state, which decays to the ground state 1S_0 via 3P_1 . We estimate that 6 μs is required to reach less than 10^{-3} remaining population in 3P_0 . About 3% of the population will decay to 3P_2 , which is repumped using the 3P_2 to 3S_1 transition at 770 nm [36]. The 3D_1 light shift can also be used to control which atoms are depumped. Pumping of unwanted atoms is suppressed by $(\Delta/\Gamma)^2 \approx 10^{-6}$; as this error is incurred at most $m = 5$ –10 times, it remains at a tolerable level.

At the end of a round, the entangled atoms are transported out of the cavity and into a computation zone with other logical qubits. At the same time, a new array is loaded into the cavity, so the entanglement sequence begins again after t_{move} .

To estimate the magnitude of the optical power needed to generate a light shift of $\Delta = 2000g$, we use the experimentally measured lifetime of the $6s8p$ 3P_1 state of 140(20) ns [77], and an estimated branching ratio of 0.3 to the 3D_1 state. Using a detuning of 1 GHz [63], we arrive at an estimate of 20 μW /site, assuming a $1/e^2$ beam radius $w_0 = \lambda$. Several other excited states could be used for light shifts, including the $6s7p$ states (730-nm transition from 3D_1) or $6s5f$ 3F_2 (528 nm). The latter state has a

stronger matrix element to 3D_1 (26-ns lifetime [77], estimated branching ratio of 90% to 3D_1), which could reduce the needed power to approximately 1.5 μW per site.

APPENDIX B: CAVITY PARAMETERS

The twisted, running-wave cavity in this work accomplishes two objectives. First, the running-wave nature reduces fast gradients in the atom-cavity coupling strength, enabling higher-fidelity spin-photon entanglement. Second, twisting the cavity gives rise to circularly polarized eigenmodes and lifts the degeneracy between the copropagating modes with σ^+ and σ^- polarization, by an amount that can be controlled by the twist angle. This allows maximum strength coupling to both σ^+ and σ^- transitions simultaneously, allowing spin-polarization entanglement to be generated in the time it takes to emit one photon.

The design of the cavity is based on several principles. First, we constrain the atom-mirror distance to be larger than 1 cm to avoid deleterious effects on the Rydberg states of atoms near the mirror surfaces. This distance is comparable to the atom-window separation in many current experiments [42]. We also want a small mode waist, to realize a large atom-cavity coupling strength, and a twist angle that enables a splitting of 100–150 MHz between σ^+ and σ^- modes in the same propagation direction, which is compatible with bias magnetic fields in the range of 60–100 G.

One example of a cavity satisfying these conditions is shown in Fig. 1(b). It is made of four mirrors: two convex mirrors with radius of curvature $R = 1.27$ cm, and two concave mirrors with $R = -1.27$ cm. The geometry is derived from a planar ring cavity with equal short and long arm lengths, and an opening angle of 11° , with an additional 11° twist out of the plane. The mirror diameter is 3 mm to satisfy geometric constraints. The mode is circular at the position of the atoms with a waist of $w_0 = 10.0$ μm . The round-trip length is $L = 6.96$ cm, corresponding to a free spectral range of 4.3 GHz and a splitting between the copropagating circularly polarized modes of 133 MHz. We note that planar ring cavities with a similar value of w_0/λ have recently been demonstrated with $\mathcal{F} \approx 51\,000$ [47].

1. Twisted cavity

The cavity has four resonance modes in the fundamental transverse mode (TEM₀₀) for each longitudinal mode number, corresponding to two polarizations (σ^+ and σ^-), and clockwise (CW) and counterclockwise (CCW) propagation directions. For a nonzero twist angle θ , the polarization of light rotates in each round trip, which manifests as a phase shift with opposite sign for σ^\pm , splitting their resonance frequencies. However, the CW σ^\pm mode is degenerate with the CCW σ^\mp mode, as required by time-reversal symmetry. Therefore, if we align the atomic σ^+

and σ^- transition frequencies with the two cavity frequencies, both transitions will decay via emission of photons in the same direction. Here, the time-reversal symmetry is broken by the magnetic field. If the direction of \vec{B} is reversed, the emission direction will also reverse.

If the mirror coatings are birefringent, the eigenmodes are no longer perfectly circularly polarized. This effect can be minimized through the use of appropriately designed coatings, and very high levels of circular polarization have been demonstrated [78]. If the polarization is elliptical, some photon emission will go into modes propagating in the opposite direction. As these photons leave the cavity through a different port, this only affects the entanglement rate, but not the fidelity.

2. Atom-cavity coupling strength

In a Fabry-Perot cavity, the cooperativity for a two-level atom at the maximum of the electric field is given by $C_{fp} = 24\mathcal{F}/(\pi k^2 w_0^2)$ [79], where \mathcal{F} is the cavity finesse $\mathcal{F} = \pi c/(L\kappa)$, $k = 2\pi/\lambda$, w_0 is the cavity waist, and L is the mirror separation. In a running-wave cavity, the cooperativity is lower by a factor of 4, because of the absence of constructive interference between the forward and return beams [47]. Therefore, we have $C = 6\mathcal{F}/(\pi k^2 w_0^2)$, but now with $\mathcal{F} = 2\pi c/(L\kappa)$, where L is the cavity round trip length. In a multilevel atom, this is further reduced by the branching ratio R_{br} from the target excited state to the target ground state. We derive the atom-cavity coupling strength g using the relation $C = 4g^2/(\kappa\Gamma)$, where Γ is the atomic transition decay rate (total decay rate, not corrected for R_{br}). This yields

$$g = \sqrt{\frac{3cR_{br}\Gamma}{k^2 w_0^2 L}}. \quad (\text{B1})$$

APPENDIX C: FIDELITY SIMULATIONS

To estimate the achievable entanglement rate and the contribution of various imperfections to the resulting state fidelity, we perform simulations of the atom-cavity system using the Lindblad master equation. We consider the simplified level diagram in Fig. 6(a), described by the Hamiltonian

$$\begin{aligned} H = & \Delta(|0_e\rangle\langle 0_e| + |1_e\rangle\langle 1_e|) \\ & + g(|0_e\rangle\langle 0|a_- + |0\rangle\langle 0_e|a_-^\dagger + |1_e\rangle\langle 1|a_+ + |1\rangle\langle 1_e|a_+^\dagger) \\ & + \frac{\Omega(t)}{2}(|0_e\rangle\langle 0_g| + |0_g\rangle\langle 0_e| + |1_e\rangle\langle 1_g| + |1_g\rangle\langle 1_e|). \end{aligned} \quad (\text{C1})$$

Here, Δ is a detuning of the atomic transitions with respect to the cavity resonance (i.e., from Doppler shifts, or from a deliberate light shift), and $\Omega(t)$ is the Rabi frequency of

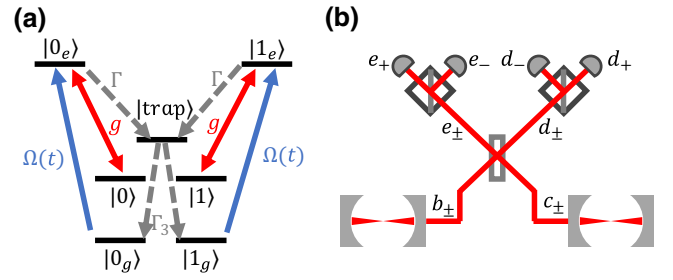


FIG. 6. Fidelity simulation. (a) Simplified level diagram used in the fidelity simulation. (b) Schematic of the photon measurement apparatus.

the two-photon excitation pulse (the intermediate state is not included explicitly).

We include the jump operators

$$\begin{aligned} c_1 &= \sqrt{\Gamma(1 - R_{br})}|\text{trap}\rangle\langle 0_e|, \\ c_2 &= \sqrt{\Gamma(1 - R_{br})}|\text{trap}\rangle\langle 1_e|, \\ c_3 &= \sqrt{\Gamma R_{br}}|0\rangle\langle 0_e|, \\ c_4 &= \sqrt{\Gamma R_{br}}|1\rangle\langle 1_e|, \\ c_5 &= \sqrt{\kappa}a_-, \\ c_6 &= \sqrt{\kappa}a_+, \\ c_7 &= \sqrt{\Gamma_3/2}|0_g\rangle\langle \text{trap}|, \\ c_8 &= \sqrt{\Gamma_3/2}|1_g\rangle\langle \text{trap}|, \end{aligned}$$

where $|\text{trap}\rangle$ is a simplified representation of the 3P_1 manifold, and has equal probability of decaying into either ground state, $|0_g\rangle$ or $|1_g\rangle$. We take the cavity output field to be $a_{\text{out},\pm} = \sqrt{\kappa}a_{\pm}$, following the input-output formalism [80].

1. Bell pair fidelity

The successful generation of Bell pairs is heralded by coincident two-photon detection in the measurement apparatus shown in Fig. 6(b). The output modes are related to the input modes using the beam-splitter relation [81]:

$$\begin{pmatrix} d_{\pm} \\ e_{\pm} \end{pmatrix} = \begin{pmatrix} \cos \xi & -e^{-i\phi} \sin \xi \\ e^{i\phi} \sin \xi & \cos \xi \end{pmatrix} \begin{pmatrix} b_{\pm} \\ c_{\pm} \end{pmatrix}. \quad (\text{C2})$$

A coincidence between d_+ and e_- or e_+ and d_- heralds the Bell state $|\psi^-\rangle = (|10\rangle - |01\rangle)/\sqrt{2}$, while a coincidence between d_+ and d_- or e_+ and e_- heralds $|\psi^+\rangle$. Imperfections in the experiment give rise to a faulty atomic state, with an error probability that depends on the detection time of the photons. We determine this from simulation by evaluating the expectation values of the stabilizers of

the Bell state as a function of the photon detection times, using the quantum regression theorem [80] as implemented in QuTIP [82]. We first consider Bell state $|\psi^-\rangle$, evaluating the following two-time correlation functions involving photon detection and the Pauli operators X_i, Z_i acting on the qubit subspace $\{|0\rangle, |1\rangle\}$ on the i th qubit:

$$P(t_1, t_2) = \langle d_+^\dagger(t_1)e_-^\dagger(t_2)e_-(t_2)d_+(t_1) \rangle,$$

$$XX(t_1, t_2) = \langle d_+^\dagger(t_1)e_-^\dagger(t_2)X_1(t_2)X_2(t_2)e_-(t_2)d_+(t_1) \rangle,$$

$$ZZ(t_1, t_2) = \langle d_+^\dagger(t_1)e_-^\dagger(t_2)Z_1(t_2)Z_2(t_2)e_-(t_2)d_+(t_1) \rangle,$$

$$L(t_1, t_2) = \langle d_+^\dagger(t_1)e_-^\dagger(t_2)Z_1^2(t_2)Z_2^2(t_2)e_-(t_2)d_+(t_1) \rangle.$$

Here, $P(t_1, t_2)$ is the probability density for a coincidence event to occur at times (t_1, t_2) , XX and ZZ are the expectation values of the same probability multiplied by the X_1X_2 and Z_1Z_2 stabilizers, and L is the detection probability multiplied by the population in the qubit subspace. The ideal value of the X_1X_2 stabilizer is -1 , which allows us to define a probability of remaining in the qubit subspace and having a Z error on the Bell state, conditioned on detecting a photon at (t_1, t_2) :

$$p_z(t_1, t_2) = \frac{1}{2} \left[1 + \frac{XX(t_1, t_2)}{P(t_1, t_2)} \frac{L(t_1, t_2)}{P(t_1, t_2)} \right]. \quad (\text{C3})$$

We can analogously define the probability of an X error in the qubit subspace, p_x , and the probability of a leakage error, p_l , as

$$p_x(t_1, t_2) = \frac{1}{2} \left[1 + \frac{ZZ(t_1, t_2)}{P(t_1, t_2)} \frac{L(t_1, t_2)}{P(t_1, t_2)} \right], \quad (\text{C4})$$

$$p_l(t_1, t_2) = \left[1 - \frac{L(t_1, t_2)}{P(t_1, t_2)} \right]. \quad (\text{C5})$$

Finally, the total probability of each type of error is determined by the weighted average:

$$P_z = \frac{1}{\mathcal{N}} \iint p_z(t_1, t_2) P(t_1, t_2) dt_1 dt_2 \quad (\text{C6})$$

with $\mathcal{N} = \iint P(t_1, t_2) dt_1 dt_2$. An analogous definition follows for P_x, P_l , and the total error probability is the sum of all three types of errors. The plots in Fig. 3 show $P_z + P_x + P_l$, while Eqs. (C3)–(C5) are used to generate the plots in Figs. 4(a)–(c).

Analogous expressions can be defined for the $|\psi^+\rangle$ Bell state with the opposite coincidence pattern in modes d_+, d_- . However, they are the same up to the expected sign of the X_1X_2 stabilizer in Eq. (C3), so we do not consider this case separately.

- [1] C. Gidney and M. Ekerå, How to factor 2048 bit RSA integers in 8 hours using 20 million noisy qubits, *Quantum* **5**, 433 (2021).
- [2] M. E. Beverland, P. Murali, M. Troyer, K. M. Svore, T. Hoefler, V. Kliuchnikov, G. H. Low, M. Soeken, A. Sundaram, and A. Vashchillo, Assessing requirements to scale to practical quantum advantage, [arXiv:2211.07629](https://arxiv.org/abs/2211.07629).
- [3] R. V. Meter, W. J. Munro, K. Nemoto, and K. M. Itoh, Arithmetic on a distributed-memory quantum multicompiler, *ACM J. Emerg. Technol. Comput. Syst.* **3**, 2:1 (2008).
- [4] C. Monroe, R. Raussendorf, A. Ruthven, K. R. Brown, P. Maunz, L. M. Duan, and J. Kim, Large-scale modular quantum-computer architecture with atomic memory and photonic interconnects, *Phys. Rev. A* **89**, 022317 (2014).
- [5] N. H. Nickerson, J. F. Fitzsimons, and S. C. Benjamin, Freely scalable quantum technologies using cells of 5-to-50 qubits with very lossy and noisy photonic links, *Phys. Rev. X* **4**, 041041 (2014).
- [6] Y. Li and S. C. Benjamin, Hierarchical surface code for network quantum computing with modules of arbitrary size, *Phys. Rev. A* **94**, 042303 (2016).
- [7] D. Gottesman and I. L. Chuang, Demonstrating the viability of universal quantum computation using teleportation and single-qubit operations, *Nature* **402**, 390 (1999).
- [8] S. Olmschenk, D. N. Matsukevich, P. Maunz, D. Hayes, L.-M. Duan, and C. Monroe, Quantum teleportation between distant matter qubits, *Science* **323**, 486 (2009).
- [9] W. Pfaff, B. J. Hensen, H. Bernien, S. B. van Dam, M. S. Blok, T. H. Taminiau, M. J. Tiggelman, R. N. Schouten, M. Markham, D. J. Twitchen, and R. Hanson, Unconditional quantum teleportation between distant solid-state quantum bits, *Science* **345**, 532 (2014).
- [10] K. S. Chou, J. Z. Blumoff, C. S. Wang, P. C. Reinhold, C. J. Axline, Y. Y. Gao, L. Frunzio, M. H. Devoret, L. Jiang, and R. J. Schoelkopf, Deterministic teleportation of a quantum gate between two logical qubits, *Nature* **561**, 368 (2018).
- [11] S. Storz, *et al.*, Loophole-free Bell inequality violation with superconducting circuits, *Nature* **617**, 265 (2023).
- [12] R. Sahu, L. Qiu, W. Hease, G. Arnold, Y. Minoguchi, P. Rabl, and J. M. Fink, Entangling microwaves with light, *Science* **380**, 718 (2023).
- [13] S. Meesala, D. Lake, S. Wood, P. Chiappina, C. Zhong, A. D. Beyer, M. D. Shaw, L. Jiang, and O. Painter, Quantum entanglement between optical and microwave photonic qubits, [arXiv:2312.13559](https://arxiv.org/abs/2312.13559).
- [14] D. L. Moehring, P. Maunz, S. Olmschenk, K. C. Younge, D. N. Matsukevich, L. M. Duan, and C. Monroe, Entanglement of single-atom quantum bits at a distance, *Nature* **449**, 68 (2007).
- [15] S. Ritter, C. Nölleke, C. Hahn, A. Reiserer, A. Neuzner, M. Uphoff, M. Mücke, E. Figueroa, J. Bochmann, and G. Rempe, An elementary quantum network of single atoms in optical cavities, *Nature* **484**, 195 (2012).
- [16] J. Hofmann, M. Krug, N. Ortegel, L. Gérard, M. Weber, W. Rosenfeld, and H. Weinfurter, Heralded entanglement between widely separated atoms, *Science* **337**, 72 (2012).
- [17] H. Bernien, B. Hensen, W. Pfaff, G. Koolstra, M. S. Blok, L. Robledo, T. H. Taminiau, M. Markham, D. J. Twitchen, L. Childress, and R. Hanson, Heralded entanglement between solid-state qubits separated by three metres, *Nature* **497**, 86 (2013).

- [18] D. Hucul, I. V. Inlek, G. Vittorini, C. Crocker, S. Debnath, S. M. Clark, and C. Monroe, Modular entanglement of atomic qubits using photons and phonons, *Nat. Phys.* **11**, 37 (2014).
- [19] A. Delteil, Z. Sun, W.-b. Gao, E. Togan, S. Faelt, and A. Imamoglu, Generation of heralded entanglement between distant hole spins, *Nat. Phys.* **12**, 218 (2016).
- [20] L. J. Stephenson, D. P. Nadlinger, B. C. Nichol, S. An, P. Drmota, T. G. Ballance, K. Thirumalai, J. F. Goodwin, D. M. Lucas, and C. J. Ballance, High-rate, high-fidelity entanglement of qubits across an elementary quantum network, *Phys. Rev. Lett.* **124**, 110501 (2020).
- [21] T. van Leent, M. Bock, F. Fertig, R. Garthoff, S. Eppelt, Y. Zhou, P. Malik, M. Seubert, T. Bauer, W. Rosenfeld, W. Zhang, C. Becher, and H. Weinfurter, Entangling single atoms over 33 km telecom fibre, *Nature* **607**, 69 (2022).
- [22] V. Krutyanskiy, M. Galli, V. Krcmarsky, S. Baier, D. A. Fioretto, Y. Pu, A. Mazloom, P. Sekatski, M. Canteri, M. Teller, J. Schupp, J. Bate, M. Meraner, N. Sangouard, B. P. Lanyon, and T. E. Northup, Entanglement of trapped-ion qubits separated by 230 meters, *Phys. Rev. Lett.* **130**, 050803 (2023).
- [23] C. M. Knaut, A. Suleymanzade, Y.-C. Wei, D. R. Assumpcao, P.-J. Stas, Y. Q. Huan, B. Machielse, E. N. Knall, M. Sutula, G. Baranes, N. Sinclair, C. De-Eknamkul, D. S. Levonian, M. K. Bhaskar, H. Park, M. Lončar, and M. D. Lukin, Entanglement of nanophotonic quantum memory nodes in a telecommunication network, [arXiv:2310.01316](https://arxiv.org/abs/2310.01316).
- [24] S. Ebadi, T. T. Wang, H. Levine, A. Keesling, G. Semeghini, A. Omran, D. Bluvstein, R. Samajdar, H. Pichler, W. W. Ho, S. Choi, S. Sachdev, M. Greiner, V. Vuletić, and M. D. Lukin, Quantum phases of matter on a 256-atom programmable quantum simulator, *Nature* **595**, 227 (2021).
- [25] P. Scholl, M. Schuler, H. J. Williams, A. A. Eberharter, D. Barredo, K.-N. Schymik, V. Lienhard, L.-P. Henry, T. C. Lang, T. Lahaye, A. M. Läuchli, and A. Browaeys, Quantum simulation of 2D antiferromagnets with hundreds of Rydberg atoms, *Nature* **595**, 233 (2021).
- [26] S. J. Evered, D. Bluvstein, M. Kalinowski, S. Ebadi, T. Manovitz, H. Zhou, S. H. Li, A. A. Geim, T. T. Wang, N. Maskara, H. Levine, G. Semeghini, M. Greiner, V. Vuletić, and M. D. Lukin, High-fidelity parallel entangling gates on a neutral-atom quantum computer, *Nature* **622**, 268 (2023).
- [27] P. Scholl, A. L. Shaw, R. B.-S. Tsai, R. Finkelstein, J. Choi, and M. Endres, Erasure conversion in a high-fidelity Rydberg quantum simulator, *Nature* **622**, 273 (2023).
- [28] D. Bluvstein, H. Levine, G. Semeghini, T. T. Wang, S. Ebadi, M. Kalinowski, A. Keesling, N. Maskara, H. Pichler, M. Greiner, V. Vuletić, and M. D. Lukin, A quantum processor based on coherent transport of entangled atom arrays, *Nature* **604**, 451 (2022).
- [29] T. M. Graham, *et al.*, Multi-qubit entanglement and algorithms on a neutral-atom quantum computer, *Nature* **604**, 457 (2022).
- [30] D. Bluvstein, *et al.*, Logical quantum processor based on reconfigurable atom arrays, *Nature* **626**, 58 (2024).
- [31] T. Đorđević, P. Samutpraphoot, P. L. Ocola, H. Bernien, B. Grinkemeyer, I. Dimitrova, V. Vuletić, and M. D. Lukin, Entanglement transport and a nanophotonic interface for atoms in optical tweezers, *Science* **373**, 1511 (2021).
- [32] W. Huie, S. G. Menon, H. Bernien, and J. P. Covey, Multiplexed telecommunication-band quantum networking with atom arrays in optical cavities, *Phys. Rev. Res.* **3**, 043154 (2021).
- [33] C. B. Young, A. Safari, P. Huft, J. Zhang, E. Oh, R. Chinnarasu, and M. Saffman, An architecture for quantum networking of neutral atom processors, *Appl. Phys. B* **128**, 151 (2022).
- [34] J. Beugnon, C. Tuchendler, H. Marion, A. Gaëtan, Y. Miroshnychenko, Y. R. P. Sortais, A. M. Lance, M. P. A. Jones, G. Messin, A. Browaeys, and P. Grangier, Two-dimensional transport and transfer of a single atomic qubit in optical tweezers, *Nat. Phys.* **3**, 696 (2007).
- [35] T. G. Tiecke, J. D. Thompson, N. P. de Leon, L. R. Liu, V. Vuletić, and M. D. Lukin, Nanophotonic quantum phase switch with a single atom, *Nature* **508**, 241 (2014).
- [36] S. Ma, G. Liu, P. Peng, B. Zhang, S. Jandura, J. Claes, A. P. Burgers, G. Pupillo, S. Puri, and J. D. Thompson, High-fidelity gates and mid-circuit erasure conversion in an atomic qubit, *Nature* **622**, 279 (2023).
- [37] W. Huie, L. Li, N. Chen, X. Hu, Z. Jia, W. K. C. Sun, and J. P. Covey, Repetitive readout and real-time control of nuclear spin qubits in ^{171}Yb atoms, *PRX Quantum* **4**, 030337 (2023).
- [38] J. W. Lis, A. Senoo, W. F. McGrew, F. Rönchen, A. Jenkins, and A. M. Kaufman, Midcircuit operations using the *omg* architecture in neutral atom arrays, *Phys. Rev. X* **13**, 041035 (2023).
- [39] M. A. Norcia, *et al.*, Midcircuit qubit measurement and rearrangement in a ^{171}Yb atomic array, *Phys. Rev. X* **13**, 041034 (2023).
- [40] Y. Wu, S. Kolkowitz, S. Puri, and J. D. Thompson, Erasure conversion for fault-tolerant quantum computing in alkaline earth Rydberg atom arrays, *Nat. Commun.* **13**, 4657 (2022).
- [41] K. Sahay, J. Jin, J. Claes, J. D. Thompson, and S. Puri, High-threshold codes for neutral-atom qubits with biased erasure errors, *Phys. Rev. X* **13**, 041013 (2023).
- [42] S. Saskin, J. T. Wilson, B. Grinkemeyer, and J. D. Thompson, Narrow-line cooling and imaging of ytterbium atoms in an optical tweezer array, *Phys. Rev. Lett.* **122**, 143002 (2019).
- [43] J. P. Covey, A. Sipahigil, S. Szoke, N. Sinclair, M. Endres, and O. Painter, Telecom-band quantum optics with ytterbium atoms and silicon nanophotonics, *Phys. Rev. Appl.* **11**, 034044 (2019).
- [44] N. Schine, A. Ryou, A. Gromov, A. Sommer, and J. Simon, Synthetic Landau levels for photons, *Nature* **534**, 671 (2016).
- [45] N. Jia, A. Georgakopoulos, A. Ryou, N. Schine, A. Sommer, and J. Simon, Observation and characterization of cavity Rydberg polaritons, *Phys. Rev. A* **93**, 41802 (2016).
- [46] K. C. Cox, D. H. Meyer, N. A. Schine, F. K. Fatemi, and P. D. Kunz, Increased atom-cavity coupling and stability using a parabolic ring cavity, *J. Phys. B: At., Mol. Opt. Phys.* **51**, 195002 (2018).
- [47] Y.-T. Chen, M. Szurek, B. Hu, J. De Hond, B. Braverman, and V. Vuletić, High finesse bow-tie cavity for strong atom-photon coupling in Rydberg arrays, *Opt. Express* **30**, 37426 (2022).

- [48] N. Jia, N. Schine, A. Georgakopoulos, A. Ryou, A. Sommer, and J. Simon, Photons and polaritons in a broken-time-reversal nonplanar resonator, *Phys. Rev. A* **97**, 013802 (2018).
- [49] D. L. Moehring, M. J. Madsen, K. C. Younge, R. N. Kohn, Jr. P. Maunz, L.-M. Duan, C. Monroe, and B. B. Blinov, Quantum networking with photons and trapped atoms (invited), *J. Opt. Soc. Am. B* **24**, 300 (2007).
- [50] C. Horsman, A. G. Fowler, S. Devitt, and R. V. Meter, Surface code quantum computing by lattice surgery, *New J. Phys.* **14**, 123011 (2012).
- [51] G. S. Vasilev, D. Ljunggren, and A. Kuhn, Single photons made-to-measure, *New J. Phys.* **12**, 063024 (2010).
- [52] D. Ganapathy, *et al.*, LIGO O4 Detector Collaboration, Broadband quantum enhancement of the LIGO detectors with frequency-dependent squeezing, *Phys. Rev. X* **13**, 041021 (2023).
- [53] D. V. Reddy, R. R. Nerem, S. W. Nam, R. P. Mirin, and V. B. Verma, Superconducting nanowire single-photon detectors with 98% system detection efficiency at 1550 nm, *Optica* **7**, 1649 (2020).
- [54] D. T. Neilson, R. Frahm, P. Kolodner, C. A. Bolle, R. Ryf, J. Kim, A. R. Papazian, C. J. Nuzman, A. Gasparyan, N. R. Basavanthally, V. A. Aksyuk, and J. V. Gates, 256×256 port optical cross-connect subsystem, *J. Lightwave Technol.* **22**, 1499 (2004).
- [55] E. Timurdogan, Z. Su, R.-J. Shiue, C. V. Poulton, M. J. Byrd, S. Xin, and M. R. Watts, in *2019 Optical Fiber Communications Conference and Exhibition (OFC)* (Optica Publishing Group, Washington, D.C., United States, 2019), p. 1. <https://ieeexplore.ieee.org/document/8696994>.
- [56] S. Ma, A. P. Burgers, G. Liu, J. Wilson, B. Zhang, and J. D. Thompson, Universal gate operations on nuclear spin qubits in an optical tweezer array of ^{171}Yb atoms, *Phys. Rev. X* **12**, 021028 (2022).
- [57] A. Jenkins, J. W. Lis, A. Senoo, W. F. McGrew, and A. M. Kaufman, Ytterbium nuclear-spin qubits in an optical tweezer array, *Phys. Rev. X* **12**, 021027 (2022).
- [58] B. Merkel, K. Thirumalai, J. E. Tarlton, V. M. Schäfer, C. J. Ballance, T. P. Harty, and D. M. Lucas, Magnetic field stabilization system for atomic physics experiments, *Rev. Sci. Instrum.* **90**, 044702 (2019).
- [59] N. Schine, A. W. Young, W. J. Eckner, M. J. Martin, and A. M. Kaufman, Long-lived Bell states in an array of optical clock qubits, *Nat. Phys.* **18**, 1067 (2022).
- [60] M. A. Norcia, *et al.*, Iterative assembly of ^{171}Yb atom arrays in cavity-enhanced optical lattices, [arXiv:2401.16177](https://arxiv.org/abs/2401.16177).
- [61] H. Shibata, K. Shimizu, H. Takesue, and Y. Tokura, Ultimate low system dark-count rate for superconducting nanowire single-photon detector, *Opt. Lett.* **40**, 3428 (2015).
- [62] C. Schuck, W. H. P. Pernice, and H. X. Tang, Waveguide integrated low noise NbTiN nanowire single-photon detectors with milli-Hz dark count rate, *Sci. Rep.* **3**, 1893 (2013).
- [63] A. P. Burgers, S. Ma, S. Saskin, J. Wilson, M. A. Alarcón, C. H. Greene, and J. D. Thompson, Controlling Rydberg excitations using ion-core transitions in alkaline-earth atom-tweezer arrays, *PRX Quantum* **3**, 020326 (2022).
- [64] B. Zhang, P. Peng, A. Paul, and J. D. Thompson, A scaled local gate controller for optically addressed qubits, [arXiv:2310.08539](https://arxiv.org/abs/2310.08539).
- [65] P. Aliferis and J. Preskill, Fault-tolerant quantum computation against biased noise, *Phys. Rev. A* **78**, 052331 (2008).
- [66] J. P. Bonilla Ataides, D. K. Tuckett, S. D. Bartlett, S. T. Flammia, and B. J. Brown, The XZZX surface code, *Nat. Commun.* **12**, 2172 (2021).
- [67] M. Grassl, Th. Beth, and T. Pellizzari, Codes for the quantum erasure channel, *Phys. Rev. A* **56**, 33 (1997).
- [68] T. M. Stace, S. D. Barrett, and A. C. Doherty, Thresholds for topological codes in the presence of loss, *Phys. Rev. Lett.* **102**, 200501 (2009).
- [69] C. A. Pattison, M. E. Beverland, M. P. da Silva, and N. Delfosse, Improved quantum error correction using soft information, [arXiv:2107.13589](https://arxiv.org/abs/2107.13589).
- [70] T.-M. Zhao, H. Zhang, J. Yang, Z.-R. Sang, X. Jiang, X.-H. Bao, and J.-W. Pan, Entangling different-color photons via time-resolved measurement and active feed forward, *Phys. Rev. Lett.* **112**, 103602 (2014).
- [71] A. J. Menssen, A. Hermans, I. Christen, T. Propson, C. Li, A. J. Leenheer, M. Zimmermann, M. Dong, H. Larocque, H. Raniwala, G. Gilbert, M. Eichenfield, and D. R. Englund, Scalable photonic integrated circuits for high-fidelity light control, *Optica* **10**, 1366 (2023).
- [72] L. Jiang, J. M. Taylor, A. S. Sørensen, and M. D. Lukin, Distributed quantum computation based on small quantum registers, *Phys. Rev. A* **76**, 062323 (2007).
- [73] C. Gidney, M. Newman, A. Fowler, and M. Broughton, A fault-tolerant honeycomb memory, *Quantum* **5**, 605 (2021).
- [74] Q. Xu, J. P. B. Ataides, C. A. Pattison, N. Raveendran, D. Bluvstein, J. Wurtz, B. Vasic, M. D. Lukin, L. Jiang, and H. Zhou, Constant-overhead fault-tolerant quantum computation with reconfigurable atom arrays, [arXiv:2308.08648](https://arxiv.org/abs/2308.08648).
- [75] J. Ramette, J. Sinclair, N. P. Breuckmann, and V. Vuletić, Fault-tolerant connection of error-corrected qubits with noisy links, [arXiv:2302.01296](https://arxiv.org/abs/2302.01296).
- [76] N. P. Breuckmann and J. N. Eberhardt, Quantum low-density parity-check codes, *PRX Quantum* **2**, 21 (2021).
- [77] C. J. Bowers, D. Budker, E. D. Commins, D. DeMille, S. J. Freedman, A. T. Nguyen, S. Q. Shang, and M. Zolotarev, Experimental investigation of excited-state lifetimes in atomic ytterbium, *Phys. Rev. A* **53**, 3103 (1996).
- [78] M. Jaffé, L. Palm, C. Baum, L. Taneja, A. Kumar, and J. Simon, Understanding and suppressing backscatter in optical resonators, *Optica* **9**, 878 (2022).
- [79] H. Tanji-Suzuki, I. D. Leroux, M. H. Schleier-Smith, M. Cetina, A. T. Grier, J. Simon, and V. Vuletić, in *Advances In Atomic, Molecular, and Optical Physics*, Vol. 60 (Elsevier, Amsterdam, 2011), p. 201.
- [80] C. Gardiner and P. Zoller, *Quantum Noise: A Handbook of Markovian and Non-Markovian Quantum Stochastic Methods with Applications to Quantum Optics* (Springer Science & Business Media, Berlin, 2004).
- [81] A. Kiraz, M. Atatüre, and A. Imamoglu, Quantum-dot single-photon sources: Prospects for applications in linear optics quantum-information processing, *Phys. Rev. A* **69**, 032305 (2004).
- [82] J. Johansson, P. Nation, and F. Nori, Qutip 2: A python framework for the dynamics of open quantum systems, *Comput. Phys. Commun.* **184**, 1234 (2013).